Nano Convergence

FULL PAPER Open Access

Heterogeneous metal substitution–driven selectivity enhancement in single-phase spinel oxides for interference-free electrochemical hydrogen sulfide detection

Namhee Kim[1,2], Jeongyun Lee[1], Dasol Jin[3*], Youngmi Lee[1*] and Myung Hwa Kim[1,2*]

Abstract

Nanomaterial-based electrochemical sensors are promising tools in atmospheric chemistry, offering reliable detection of toxic gases. Here, we report a single-phase tetrametallic spinel oxide, $(Mn_{0.56}Cr_{0.77}Rh_{0.77}Ni_{0.90})O_4$ (MCRN-O), as an electrode material for amperometric H_2S sensing. Synergistic interactions among multiple cations within the spinel framework enabled homogeneous integration, imparting distinctive physicochemical properties and superior electrochemical performance. In deaerated phosphate-buffered saline solution (0.05 M), MCRN-O delivered high sensitivity (0.0084 μA μM^{-1}) and a low detection limit (0.058 μM), markedly outperforming the comparison samples MCN-O and MC-O. It also exhibited excellent selectivity, with coefficient values below −2 for CO and NO, while achieving performance comparable to or better than previously reported electrochemical H_2S sensors.

Keywords Electrochemical sensing, Hydrogen sulfide oxidation, Spinel oxide, Nanoparticle

1 Introduction

Recently, air pollution has become an increasingly serious problem in our daily lives due to rapid industrial development. Major air pollutants include nitrogen oxides (NO_x), carbon monoxide (CO), and hydrogen sulfide (H_2S), which contribute significantly to environmental contamination [1–3]. Among them, H_2S is a colorless, toxic, flammable, and combustible gas with a distinctive odor resembling that of rotten eggs [4, 5]. H_2S is commonly generated in various environments such as sewage treatment plants, oil refineries, and hot springs [6, 7]. Even at low concentrations below 5 ppm, it can cause irritation to the eyes and respiratory system [1, 8]. Exposure to concentrations above 100 ppm may result in central nervous system paralysis, and levels exceeding 500 ppm can be fatal [9]. In addition to its toxicity, H_2S is readily oxidized to sulfate ions (SO_4^{2-}), which can adversely affect the climate by influencing sunlight reflection and contributing to aerosol formation [10]. Therefore, it is crucial to develop detection systems capable of selectively and sensitively monitoring low concentrations of H_2S in real time. While various techniques such as gas chromatography and fluorescence spectroscopy have been employed for H_2S detection, these techniques

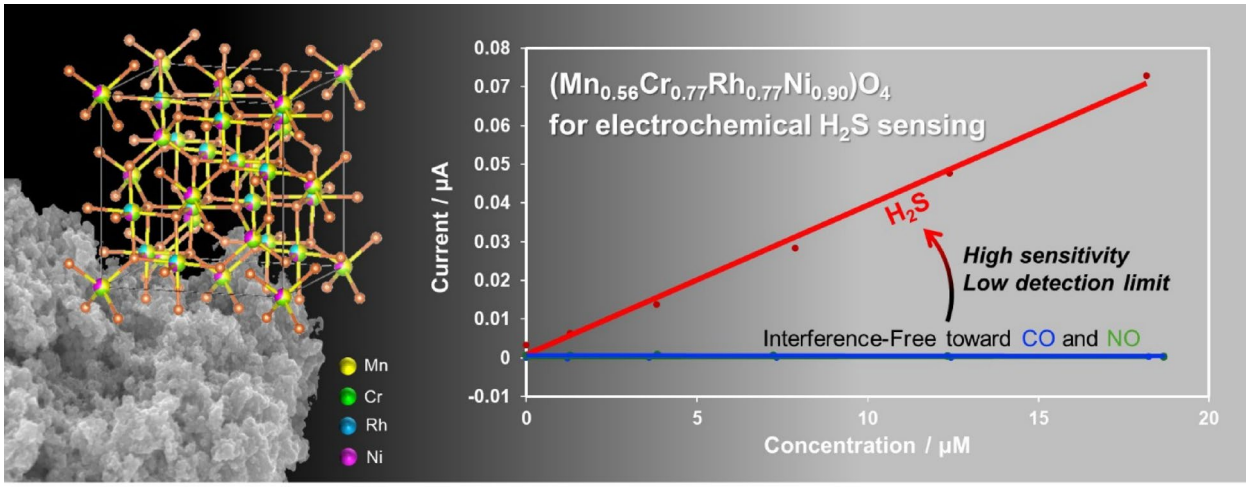
†Namhee Kim and Jeongyun Lee contributed equally to this work.

*Correspondence:
Dasol Jin
dasoljin@jbnu.ac.kr
Youngmi Lee
youngmilee@ewha.ac.kr
Myung Hwa Kim
myungkim@ewha.ac.kr

Full list of author information is available at the end of the article

© The Author(s) 2026. **Open Access** This article is licensed under a Creative Commons Attribution-NonCommercial-NoDerivatives 4.0 International License, which permits any non-commercial use, sharing, distribution and reproduction in any medium or format, as long as you give appropriate credit to the original author(s) and the source, provide a link to the Creative Commons licence, and indicate if you modified the licensed material. You do not have permission under this licence to share adapted material derived from this article or parts of it. The images or other third party material in this article are included in the article's Creative Commons licence, unless indicated otherwise in a credit line to the material. If material is not included in the article's Creative Commons licence and your intended use is not permitted by statutory regulation or exceeds the permitted use, you will need to obtain permission directly from the copyright holder. To view a copy of this licence, visit http://creativecommons.org/licenses/by-nc-nd/4.0/.

Graphical abstract



generally require complicate multi-stage protocol for quantification [11–13]. Electrochemical sensing offers distinct advantages, including simplicity, rapid response, and real-time monitoring capabilities [7, 14, 15].

Recent advances in nanomaterials highlight electrochemical signal amplification as an effective approach for improving the sensitivity and selectivity of electrochemical sensors and biosensors [16–18]. Among these, spinel oxides (AB_2O_4) are particularly attractive owing to their structural stability, compositional tunability, and catalytic activity [19–21]. In their typical structure, A^{2+} cations occupy tetrahedral sites while B^{3+} cations reside in octahedral sites, conferring unique physicochemical properties relevant to gas sensing [22, 23]. Notably, chromite spinels (MCr_2O_4, M = Zn [24], Mg [25] and Ni [26]) possess excellent crystal stability and compositional versatility, making them attractive for integration into robust, real-time detection platforms. This approach supports a wide spectrum of applications, from chemical sensing of hazardous species to biosensing of biologically relevant targets [27–29].

Herein, we present a single-phase quaternary spinel oxide MCRN-O for amperometric H_2S sensing with high selectivity and sensitivity. This nanomaterial exhibits distinctive physicochemical properties arising from synergistic interactions among multiple cations within a normal spinel oxide framework. The multimetal-substituted composition provides high sensitivity and selectivity for H_2S detection compared with the simple spinel oxide (e.g., $MnCr_2O_4$), while also exhibiting electrochemical sensing performance comparable to previously reported sensors.

2 Experimental

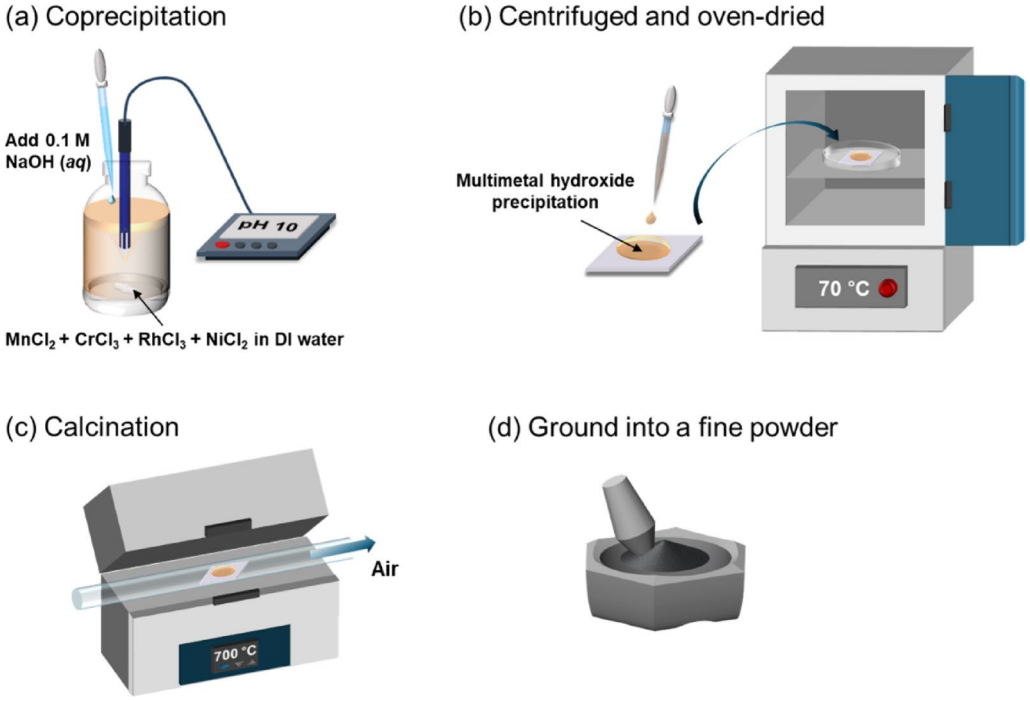
2.1 Materials

Manganese (II) chloride tetrahydrate ($MnCl_2{\cdot}4H_2O$, 99.99%), chromium (III) chloride hexahydrate ($CrCl_3{\cdot}6H_2O$, ≥ 98%), nickel chloride hexahydrate ($NiCl_2{\cdot}6H_2O$) and rhodium (III) chloride hydrate ($RhCl_3{\cdot}xH_2O$, ≥ 99.9%) were purchased from Sigma-Aldrich. Sodium hydroxide (NaOH) beads were purchased from Daejung (Korea). All chemicals were of analytical grade, and all solutions for the experiments were prepared using deionized (DI) water (resistivity ≥ 18 MΩ cm).

2.2 Synthesis

MCRN-O nanoparticles were prepared *via* multi-metal precursor co-precipitation followed by thermal annealing as Scheme 1. Specifically, $MnCl_2{\cdot}4H_2O$ (9.8 mg), $CrCl_3{\cdot}6H_2O$ (10.3 mg), $NiCl_2{\cdot}6H_2O$ (10.6 mg), and $RhCl_3{\cdot}xH_2O$ (18.6 mg) were dissolved in 10 mL of DI water and sonicated for 10 min to obtain a transparent precursor solution.

0.1 M NaOH (*aq*) was then added dropwise under moderate stirring (650 rpm) until the pH reached 10.0. The resulting precipitate was collected by centrifugation (4000 rpm, 3-cycles) and thoroughly washed with DI water to remove residues. The purified precipitate was re-dispersed in 2 mL of DI water, drop-cast onto a Si wafer, and dried at 70 °C for 24 h. Subsequent annealing was performed in air at 700 °C for 3 h, after which the product was gently ground into a fine powder. For comparison, bimetallic (MC-O) and trimetallic (MCN-O) nanoparticles were synthesized using the same



Scheme 1 Schematic illustration of synthesis procedure for the preparation of MCRN-O by multi-metal precursor co-precipitation followed by thermal annealing

procedure, employing only the corresponding two (Mn and Cr) or three (Mn, Cr, and Ni) metal precursors, respectively.

2.3 Physical characterization

Surface morphology and microstructure of the as-prepared nanomaterials were examined by field-emission scanning electron microscopy (FE-SEM; JEOL JSM-7610 F) equipped with an energy-dispersive X-ray spectrometer (EDS). Crystal structures were analyzed by X-ray diffraction (XRD; PANalytical EXPERT pro/X-ray diffractometer with Cu Kα source) and Fourier transform infrared spectroscopy (FT-IR; INVENIO-R, Bruker). Transmission electron microscopy (TEM; JEM-ARM 200 F NEOARM) coupled with energy-dispersive X-ray spectroscopy (EDS) was employed to investigate the nanostructure and elemental distribution. The surface chemical composition and oxidation states were examined through angle-resolved X-ray photoelectron spectroscopy (AR-XPS; K-ALPHA, Thermo Fisher Scientific) was performed using monochromatic Al Kα radiation (1486.6 eV). XPS peak fitting was carried out after Shirley background subtraction using constrained peak shapes and full width at half maximum values.

2.4 Electrochemical measurements

A glassy carbon (GC) disk electrode (3 mm in diameter) was polished using a polishing cloth with alumina powder and DI water. After polishing, the electrode was sonicated in DI water for 5 min to remove any residual particles. The loading solution was prepared by dispersing each synthesized nanoparticle sample in DI water at a concentration of 2 mg mL^{-1} (e.g., 5 mg catalyst dispersed in 10 mL DI water) by ultrasonication. Subsequently, 6 µL of the suspension was drop-cast onto a polished GC electrode and dried in an oven at 60 °C for 5 min. This deposition–drying step was repeated five times, resulting in a total catalyst loading of 60 µg on the GC electrode. Electrochemical measurements were performed using a three-electrode system consisting of the sample-modified GC electrode as the working electrode (WE), a coiled platinum wire as the counter electrode (CE), and a saturated calomel electrode (SCE) as the reference electrode (RE). Electrochemical analyzer (CHI 1000 A, CH Instruments, Inc.) was used to evaluate the electrochemical oxidation of H_2S. The 0.05 M phosphate-buffered saline solution (PBS, pH 7.4) was prepared by mixing sodium phosphate dibasic (Na_2HPO_4) and sodium phosphate monobasic (NaH_2PO_4). Linear sweep voltammetry (LSV) was conducted over a potential range from – 0.2 V to 0.6 V to determine the potential at which the target analyte (H_2S) is oxidized nearly exclusively without the redox reactions of potential interfering species (CO and NO). Amperometric measurements were then carried out at a fixed potential of 0.1 V. For calibration, an aliquot of a stock solution of each gas (H_2S, NO, and CO) was successively injected into deaerated PBS to alter the concentration. H_2S stock solution (3.2 mM) was prepared

by dissolving Na_2S in 0.05 M PBS pre-purged with Ar for 20 min. The stock solutions of NO (1.91 mM) and CO (0.9 mM) were prepared by purging deaerated 0.05 M PBS with NO and CO gases, respectively, for 20 min. Electrochemical impedance spectroscopy (EIS) were conducted over a frequency range from 1 MHz to 0.1 Hz in 0.05 M PBS solution. As in the other measurements, a three-electrode system was employed, with a double junction SCE used as the reference electrode.

3 Results and discussion

3.1 Physical characterization

The as-prepared $(Mn_{0.56}Cr_{0.77}Rh_{0.77}Ni_{0.90})O_4$, $(Mn_{0.32}Cr_{0.32}Ni_{0.36})O_4$, and $(Mn_{0.41}Cr_{0.59})O_x$ samples, with molar fractions determined by EDS analysis (Table S1), are hereafter referred to as MCRN-O, MCN-O and MC-O, respectively. Their phase purity and structural characteristics differ markedly, as confirmed by XRD (Fig. 1a). The MCRN-O sample shows well-resolved diffraction peaks that align with the standard pattern of $MnCr_2O_4$ normal spinel oxide (JCPDS no. 54–876), confirming the formation of a highly crystalline single-phase. In contrast, the MC-O sample shows a two-phase composition, with diffraction peaks corresponding to both $MnCr_2O_4$ and Cr_2O_3 (JCPDS no. 70-3766). Given that both samples were synthesized under identical conditions, the distinct phase behavior highlights the advantage of multi-element compositions in stabilizing the spinel lattice and promoting single-phase formation at relatively low temperatures [30–32]. Furthermore, the slight shift of the MCRN-O diffraction peaks toward higher angles indicates lattice contraction with reduced interplanar spacing, which can be attributed to the incorporation of smaller Rh and Ni cations into the MC-O lattice. The average crystallite sizes, calculated from the (311) diffraction peak at $2\theta = 35.2°$ using Scherrer's equation ($D = K\lambda / \beta\cos\theta$, where D is the crystallite size, K is the shape factor, λ is the X-ray wavelength, β is the full width at half maximum (FWHM) of the diffraction peak, and θ is the Bragg angle), were determined to be 8.02 nm for MCRN-O and 12.7 nm for MC-O. These results further confirm the presence of lattice strain and structural densification induced by heterogeneous metal substitution.

The coexistence of multiple cationic states and their heterogeneous substitution, which are expected to induce local lattice distortion and electronic redistribution, were further examined by high-resolution X-ray photoelectron spectroscopy (XPS). Although several XPS components exhibit strong spectral overlap, deconvolution was performed following standard fitting protocols using reported spin–orbit splitting, relative peak area ratios, and binding energy positions. The Mn 2p spectrum (Fig. 1b) displays peaks at 641.4 eV ($2p_{3/2}$) and 652.3 eV ($2p_{1/2}$), characteristic of Mn^{2+} [33, 34]. Additional components at ~642.0 eV and ~653.0 eV are assigned to Mn^{3+}, while shake-up satellite peaks at ~645 eV and ~655 eV confirm the coexistence of multiple Mn oxidation states [35, 36]. The Cr 2p region (Fig. 1d) exhibits two distinct doublets. The main peaks at 575.9 eV ($2p_{3/2}$) and 585.4 eV ($2p_{1/2}$) are assigned to Cr^{3+} species, whereas the secondary peaks at 578.0 eV and 587.7 eV are attributed to surface CrOOH-related species, in agreement with reported values [37, 38]. Notably, Cr^{3+} is dominantly accommodated at octahedral sites in the spinel lattice, in good agreement with previously reported values [39]. This assignment is further supported by the corresponding O 1s spectra (Fig. S2), which display a predominant lattice oxygen component centered at approximately 529 eV, along with a

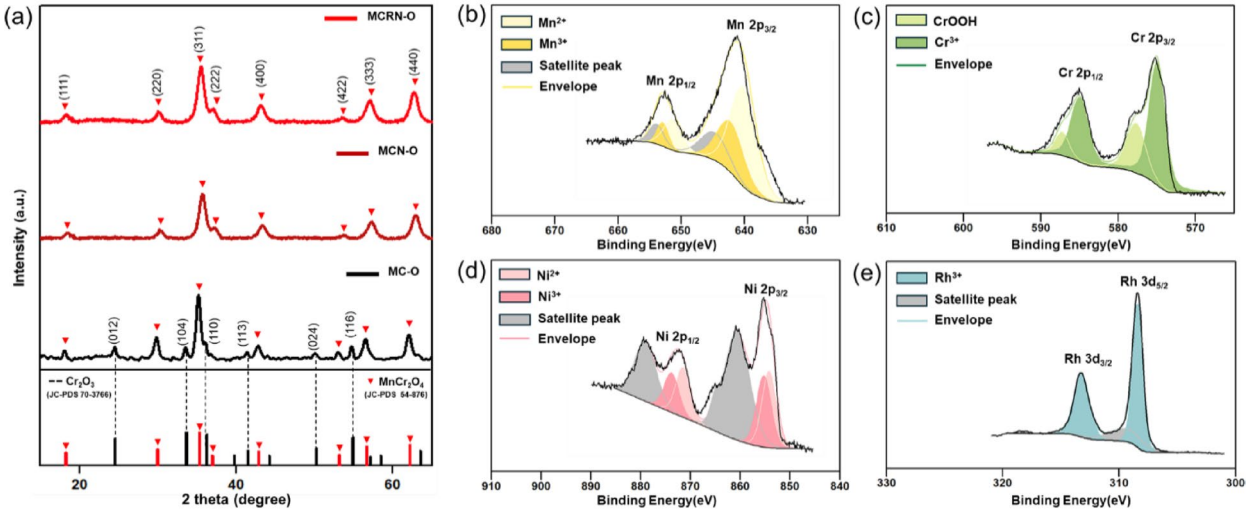


Fig. 1 **a** XRD patterns of MCRN-O, MCN-O and MC-O with the corresponding JCPDS reference patterns, and XPS spectra of MCRN-O in **b** Mn 2p, **c** Cr 2p, **d** Ni 2p and **e** Rh 3d regions

chemisorbed oxygen species at 530.4 eV [39]. The Ni 2p spectrum (Fig. 1e) reveals mixed-valence species. Peaks at 854.1 eV ($2p_{3/2}$) and 872.3 eV ($2p_{1/2}$) are assigned to Ni^{2+}, while peaks at 854.9 eV ($2p_{3/2}$) and 874.1 eV ($2p_{1/2}$) correspond to Ni^{3+} [40, 41]. The Rh 3d spectrum (Fig. 1f) shows a well-defined doublet with a spin–orbit splitting of ~5 eV. The peaks at 308.4 eV ($3d_{5/2}$) and 313.2 eV ($3d_{3/2}$) are characteristic of Rh^{3+}, indicating its exclusive presence in the oxidation state of +3 within the spinel lattice [42, 43]. Overall, XPS reveals mixed +2/+3 oxidation states for Mn and Ni, while Rh and Cr (with a minor contribution from surface-associated CrOOH species) are predominantly present as Rh^{3+} and Cr^{3+}, indicating heterogeneous multimetal substitution that induces local lattice strain and electronic redistribution. Such modulation of metal–oxygen covalency is expected to facilitate interfacial charge transfer, thereby contributing to the enhanced selectivity and catalytic efficiency of MCRN-O (*vide infra*). Although XPS alone cannot directly determine tetrahedral or octahedral site occupancy, the cation distribution is inferred from XPS-derived valence states, XRD-confirmed single-phase formation, and established literature on spinel systems. Furthermore, Fig. S1 shows the FT-IR spectrum of MCRN-O, which exhibits two absorption peaks at 480 cm^{-1} and 606 cm^{-1}. These correspond to metal–O stretching vibrations originating from octahedral and tetrahedral sites, respectively [44], a characteristic feature commonly observed in the normal spinel structure of Mn_3O_4 [45, 46].

The morphological characteristics of MCRN-O, MCN-O and MC-O were examined by SEM (Fig. 2a–c and Fig. S3). The as-prepared nanoparticles exhibit a relatively narrow particle-size distribution without noticeable large agglomerates or abnormal grain growth, indicating reasonably uniform morphology across the samples. The selected-area electron diffraction (SAED) pattern of MCRN-O displays distinct diffraction rings, indicating a polycrystalline nature (Fig. 2d) and supporting the formation of a well-crystallized spinel-type oxide structure [47]. The HRTEM image displays well-resolved lattice fringes with interplanar spacings of 0.256, 0.164, and 0.150 nm, corresponding to the (311), (333), and (440) planes of the spinel structure of MCRN-O, respectively, confirming the formation of crystalline spinel oxide (Fig. 2e). TEM–EDS elemental mapping demonstrates a homogeneous distribution of all five metallic components throughout the nanoparticles (Fig. 2f). In addition, EDS measurements were performed at 10 different regions for each sample to ensure statistical reliability (Table S1). For all samples, including the representative MCRN-O, the measured atomic percentages closely match the stoichiometric mole fractions with negligible standard deviations, indicating highly uniform elemental distribution and good compositional reproducibility across the measured areas.

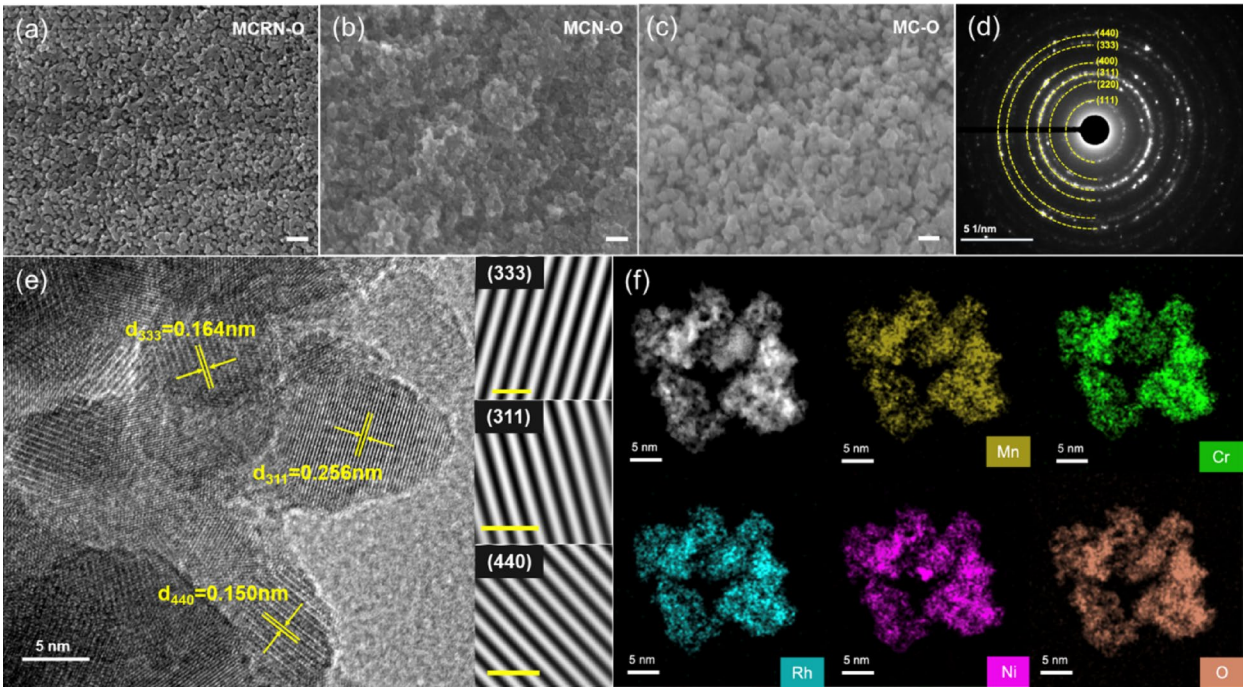


Fig. 2 SEM images of **a** MCRN-O, **b** MCN-O and **c** MC-O. TEM characterization of MCRN-O nanoparticles: **d** SAED pattern, **e** HRTEM image with lattice fringe analysis and **f** EDS elemental mapping

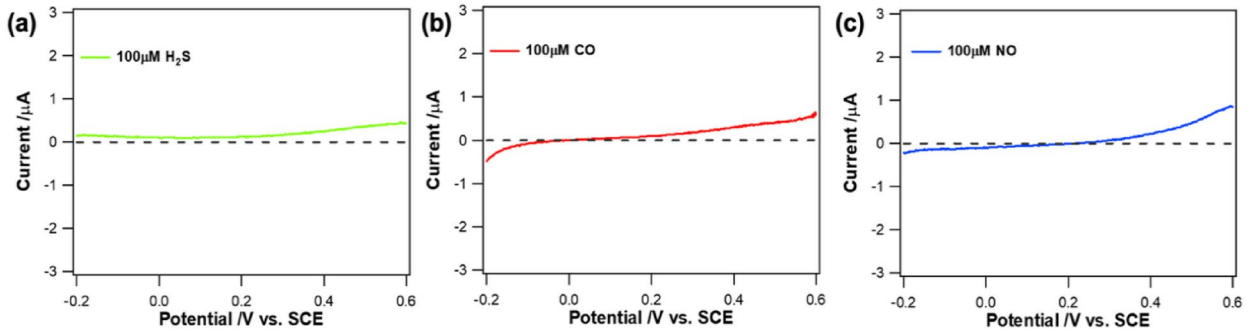


Fig. 3 Background-corrected LSV curves of MCRN-O in 0.05 M PBS containing 100 μM **a** H_2S, **b** CO, and **c** NO acquired at a scan rate of 10 mV s^{-1}

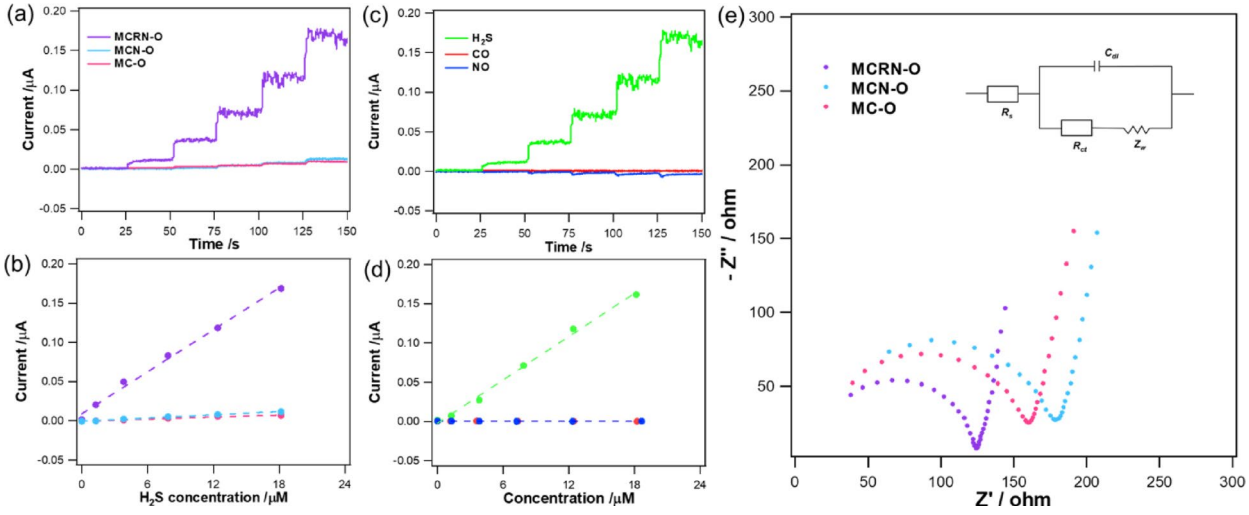


Fig. 4 **a** Amperometric current responses of MCRN-O, MCN-O and MC-O with successive increase of H_2S concentration (0–18 μM), and **b** the corresponding calibration curves. **c** Amperometric current responses of MCRN-O to the concentration changes of H_2S, CO, and NO obtained independently, and **d** the corresponding calibration plots. **e** Nyquist plots of MCRN-O, MCN-O and MC-O (inset: equivalent circuit model for EIS analysis). All measurements were conducted at an applied potential of 0.1 V (vs. SCE) in deaerated 0.05 M PBS solution

3.2 Electrochemical characterization

Linear sweep voltammetry (LSV) and amperometric analyses were conducted to systematically evaluate the electrochemical responses of electrodes toward CO, NO and H_2S. The background-corrected LSV profiles recorded in 100 μM solutions of the sensing analytes are presented in Fig. 3 for MCRN-O, Fig. S4 for MCN-O and Fig. S5 for MC-O. Based on these LSV results, 0.1 V versus SCE was identified as the optimal operating potential for H_2S oxidation, providing minimal interference from the redox responses of CO and NO. As summarized in Table S2, additional validation using MCRN-O identifies 0.1 V as the optimal potential, providing the best balance between H_2S sensitivity and selectivity against competing gaseous interferents, compared with lower (0.05 V) and higher (0.2 and 0.3 V) potential regions for H_2S sensing. Thus, an applied potential of 0.1 V (vs. SCE) was employed for amperometric measurement in this study. During the LSV and amperometric experiments, a gas-tight electrochemical cell was used and maintained in an Ar-saturated state to prevent unintended side reactions.

Figure 4a shows the dynamic current responses to H_2S concentration changes obtained with MCRN-O, MCN-O and MC-O. The corresponding calibration curves (Fig. 4b) verify that the measured currents at the respective electrode materials are linearly proportional to the H_2S concentration while MCRN-O exhibits a greatly higher sensitivity (0.0084 μA $μM^{-1}$) compared with MCN-O (0.00074 μA $μM^{-1}$) and MC-O (< 0.0002 μA $μM^{-1}$).

To elucidate whether the sensing response is governed by electron-transfer kinetics or mass-transport processes, amperometric measurements were conducted under systematically controlled applied potentials and rotation speeds. As shown in Fig. S6(a), response times were compared at different applied potentials while maintaining a constant magnetic stirrer rotation speed of approximately 1350 rpm. For the amperometric

measurements, the solution (PBS) was magnetically stirred to homogenize the injected H_2S. The response time decreased progressively with increasing anodic potential, indicating that the sensing behavior is partially governed by electron-transfer kinetics. Furthermore, as presented in Fig. S6(b), response times were evaluated as a function of rotation speed. A significantly shorter response time was observed at a higher rotation speed (2500 rpm) compared to that at a lower speed (150 rpm), demonstrating a pronounced dependence on mass transport. Taken together, these results confirm that the H_2S sensing performance of MCRN-O arises from a coupled contribution of electron-transfer kinetics and diffusion-controlled mass transfer, rather than from a purely surface-controlled or exclusively diffusion-limited process.

In addition, the current values of MCRN-O measured at the same applied potential of 0.1 V (vs. SCE) were barely changed responding to the varied concentrations of CO and NO (Fig. 4c). The mean sensitivity slopes (± standard deviations) determined from five different measurements are as follows: 0.0084 μA μM^{-1} (± 0.00046) for H_2S, -8.5×10^{-7} μA μM^{-1} ($\pm 1.85\times10^{-5}$) for CO, and -6.5×10^{-5} μA μM^{-1} ($\pm 4.2\times10^{-5}$) for NO (Fig. 4d). NO was slightly reduced at the selected applied potential (0.1 V vs. SCE) while CO elicited virtually no current response. However, the current response to NO was insignificant compared to that to H_2S. In fact, MCRN-O successfully oxidizes H_2S solely with negligible interference from the redox reactions of CO and NO, indicating the high selectivity to H_2S. The amperometric selectivity coefficient for H_2S against CO or NO was calculated using equation below:

$$\log K^{\mathrm{amp}}_{\mathrm{H?S},i} = \log\left(\frac{\text{sensitivity to } i}{\text{sensitivity to H?S}}\right)$$

where i is CO or NO. The values of were $\log K^{\mathrm{amp}}_{\mathrm{H?S},i}$ – 2.11 for NO and –3.99 for CO, indicating extremely high selectivity of MCRN-O to H_2S.

Figure 4e shows the Nyquist plots of MCRN-O, MCN-O and MC-O obtained from electrochemical impedance spectroscopy (EIS) experiments. The applied potential was set at 0.1 V (vs. SCE), consistent with the potential used in the amperomtric measurements. The Nyquist plot, reflecting the complex impedance characteristics of the electrode–electrolyte interface, quantitatively elucidates the charge-transfer kinetics and interfacial processes that dictate the overall electrochemical performance. Notably, MCRN-O exhibited a smaller charge transfer resistance (R_{ct}) than MCN-O and MC-O. This indicates that MCRN-O more effectively facilitates the oxidation of H_2S with faster electron transfer rate compared to the other samples which can be correlated with its higher amperometric sensitivity [48].

Electrode-to-electrode reproducibility is a critical metric for practical H_2S sensing applications. In this regard, a single MCRN-O–modified electrode was further evaluated under continuous H_2S exposure (Fig. 5a), exhibiting stable current responses with negligible signal degradation. In addition, reproducibility was assessed using four independently prepared electrodes (Fig. 5b), which showed consistent sensitivities with only minor deviations. These results confirm the good operational stability and reproducibility of the MCRN-O sensor, further supporting its practical applicability for the rational design of future gas-sensing materials.

The non-faradaic charging currents of the as-prepared spinel oxide nanoparticle series were measured by cyclic voltammetry (CV) in 1 M KNO_3 at various scan rates (Figs. S7a–c). The double-layer capacitance (C_{dl}), which reflects the electrochemically active surface area (ECSA), was determined by linear fitting ($R^2 = 0.9998$) of the difference between anodic and cathodic charging currents

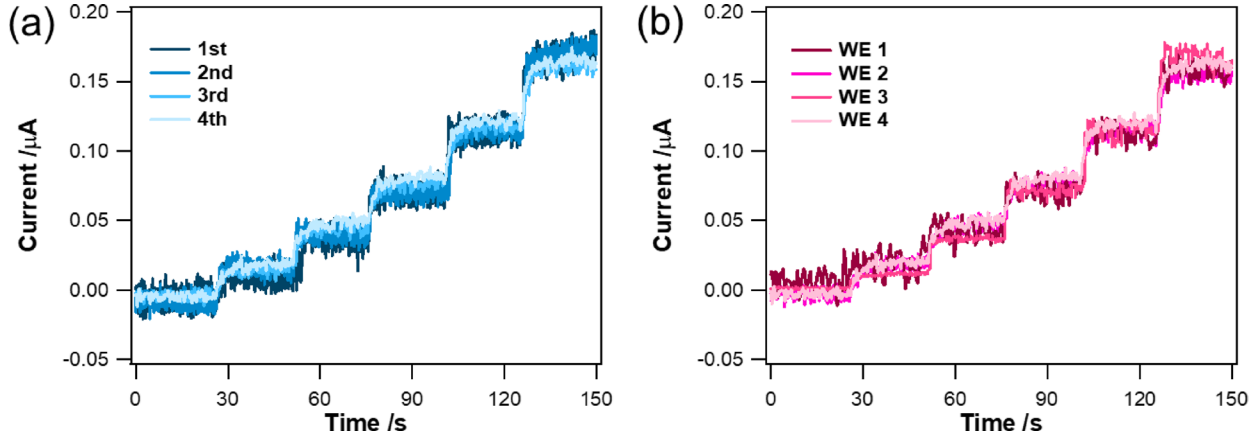


Fig. 5 Amperometric current responses of MCRN-O to successive additions of H_2S (0–18 μM) obtained a during continuous operation using a single electrode and b using different electrodes to evaluate reproducibility

Table 1 Comparison of the sensitivity and LOD values of as-prepared materials with those of the other amperometric H_2S sensors

Sensing material	Sensitivity (μA $μM^{-1}$)	Limit of detection (μM)	Working electrode	Reference
MCRN-O	0.0084	0.058	GCE (3 mm)	This work
MCN-O	0.0007	0.513	GCE (3 mm)	This work
MC-O	0.0002	0.237	GCE (3 mm)	This work
GCE/poly-o–PD	0.00028	0.015	GCE (3 mm)	[50]
POPD/RGO-MoS_2/GCE	0.0008	0.01	GCE (3 mm)	[51]
SWCNTs-PVA	0.0094	34	Au disk (1 mm)	[52]
IrP_2	0.0307	0.13	GCE (3 mm)	[53]
Graphene-Based 3D Scaffold	0.0192	0.05	Nickel form	[54]

(Δi_c) at the mid-potential as a function of scan rate (Fig. S7d). The slope of the resulting linear fit corresponds to C_{dl}, which is proportional to the ECSA [49]. Based on this analysis, MCRN-O was found to exhibit a substantially higher ECSA, being 37.9 and 87.8 times greater than those of MCN-O and MC-O, respectively. This trend is consistent with the amperometric sensitivity results (*vide supra*), reinforcing the correlation between ECSA and electrochemical activity. Collectively, these results demonstrate that MCRN-O possesses the largest ECSA, thereby contributing to its enhanced H_2S sensing sensitivity.

Table 1 summarizes the sensitivity and limit of detection (LOD) values for various H_2S sensing materials reported in previous studies. In addition to the significantly higher sensitivity, MCRN-O demonstrates a much lower LOD of 0.058 μM than MCN-O (0.513 μM) and MC-O (0.237 μM). The LOD values were calculated using the widely accepted criterion of a signal-to-noise ratio (S/N) of 3. The lower the LOD, the better the capability to detect trace amounts of an analyte, which is crucial for applications requiring sensitive monitoring. In fact, the sensing performance of MCRN-O was better or comparable to the sensors found in the literature. In particular, MCRN-O exhibited very LOD compared to the sensors with a similar sensitivity, highlighting its enhanced capability for low-level H_2S detection.

4 Conclusions

In this study, we demonstrated the applicability of MCRN-O as an effective electrode material for amperometric H_2S sensing. Due to synergistic interactions among multiple cations within the normal spinel oxide framework, characterized by predominantly + 3 oxidation states for Rh and Cr and mixed + 2/+3 oxidation states for Ni and Mn, the tetrametallic components are homogeneously incorporated, resulting in enhanced electrochemical properties. As a result, MCRN-O exhibited high sensitivity (0.0084 μA $μM^{-1}$) and a low detection limit (0.058 μM) toward H_2S, significantly outperforming the simple spinel oxide MC-O (0.0002 μA $μM^{-1}$ and 0.237 μM). Moreover, MCRN-O displayed excellent selectivity, with selectivity coefficient values below − 2 for both CO and NO, while maintaining sensing performance comparable to previously reported sensors.

Supplementary Information

The online version contains supplementary material available at https://doi.org/10.1186/s40580-026-00539-z.

Supplementary Material 1

Acknowledgements
D.J. gratefully acknowledge support from Department of Chemistry, College of Natural Science at Jeonbuk National University.

Authors' contributions
Y.L., M.H.K. and D.J. conceptualized and supervised the research. N.K. and J.L performed the measurements, curated the data and prepared the visualizations. N.K., J.L., and D.J. conducted validation. M.H.K., Y.L., N.K., J.L and D.J. cowrote the manuscript.

Funding
This work was financially supported by the National Research Foundation of Korea (NRF) funded by the Ministry of Science and ICT or by the Ministry of Education (NRF-RS-2018-NR031064 and RS-2025-16063688 for MHK, NRF-RS-2023-NR076977 for YL).

Data availability
Data will be made available on request.

Declarations

Competing interests
The authors declare no competing financial interests.

Author details
[1]Department of Chemistry and Nanoscience, Ewha Womans University, Seoul 03760, Republic of Korea
[2]Institute of Multiscale Matter and System (IMMS), Ewha Womans University, Seoul 03760, Republic of Korea
[3]Department of Chemistry, Jeonbuk National University, Jeonju 54896, Republic of Korea

Received: 31 October 2025 / Accepted: 12 February 2026
Published online: 23 February 2026

References

1. X. Yang et al., Nafion-based amperometric H_2S sensor using Pt-Rh/C sensing electrode. Sens. Actuators B Chem. **273**, 635 (2018). https://doi.org/10.1016/j.snb.2018.06.087
2. I. Romanytsia, J.-P. Viricelle, P. Vernoux, C. Pijolat, Application of advanced morphology Au–X (X=YSZ, ZrO_2) composites as sensing electrode for solid state mixed-potential exhaust NO_x sensor. Sens. Actuators B Chem. **207**, 391 (2015). https://doi.org/10.1016/j.snb.2014.10.017
3. Y. Guan et al., Highly sensitive amperometric Nafion-based CO sensor using Pt/C electrodes with different kinds of carbon materials. Sens. Actuators B Chem. **239**, 696 (2017). https://doi.org/10.1016/j.snb.2016.08.034

4. G.M. Hingangavkar, S.A. Kadam, Y.-R. Ma, R.N. Mulik, V.B. Patil, Highly selective and sensitive MoS_2 nano-sensor for H_2S detection. J. Alloys Compd. **941**, 168849 (2023). https://doi.org/10.1016/j.jallcom.2023.168849
5. L. Liu, Y. Wang, Y. Dai, G. Li, S. Wang, T. Li, T. Zhang, S. Qin, In situ growth of NiO@SnO_2 hierarchical nanostructures for high performance H_2S sensing. ACS Appl. Mater. Interfaces **11**, 44829 (2019). https://doi.org/10.1021/acsami.9b13001
6. M.A. Khan, F. Qazi, Z. Hussain, M.U. Idrees, S. Soomro, S. Soomro, Recent trends in electrochemical detection of NH_3, H_2S and NO_x gases. Int. J. Electrochem. Sci. **12**, 1711 (2017). https://doi.org/10.20964/2017.03.76
7. F. Paré, R. Castro, D. Gabriel, X. Guimerà, G. Gabriel, M. Baeza, Feasible H_2S sensing in water with a printed amperometric microsensor. ACS ES T Water **3**, 1116 (2023). https://doi.org/10.1021/acsestwater.2c00589
8. C. Szabo, C. Ransy, K. Módis, M. Andriamihaja, B. Murghes, C. Coletta, G. Olah, K. Yanagi, F. Bouillaud, Regulation of mitochondrial bioenergetic function by hydrogen sulfide. Part I. Biochemical and physiological mechanisms. Br. J. Pharmacol. **171**, 2099 (2014). https://doi.org/10.1111/bph.12369
9. C. Huang, D. Liu, D. Wang, H. Guo, T. Thomas, J.P. Attfield, F. Qu, S. Ruan, M. Yang, Mesoporous $Ti_{0.5}Cr_{0.5}N$ for trace H_2S detection with excellent long-term stability. J. Hazard. Mater. **423**, 127193 (2022). https://doi.org/10.1016/j.jhazmat.2021.127193
10. W. Li et al., Amperometric H_2S sensor based on a Pt-Ni alloy electrode and a proton conducting membrane. Sens. Actuators B Chem. **311**, 127900 (2020). https://doi.org/10.1016/j.snb.2020.127900
11. S.K. Pandey, K.-H. Kim, K.-T. Tang, A review of sensor-based methods for monitoring hydrogen sulfide. TrAC Trends Anal. Chem. **32**, 87 (2012). https://doi.org/10.1016/j.trac.2011.08.008
12. N. Jornet-Martínez, L. Hakobyan, A.I. Argente-García, C. Molins-Legua, P. Campíns-Falcó, Nylon-supported plasmonic assay based on the aggregation of silver nanoparticles: in situ determination of hydrogen sulfide-like compounds in breath samples as a proof of concept. ACS Sens. **4**, 2164 (2019). https://doi.org/10.1021/acssensors.9b01019
13. M. Dulac, A. Melet, E. Galardon, Reversible detection and quantification of hydrogen sulfide by fluorescence using the hemoglobin I from *Lucina pectinata*. ACS Sens. **3**, 2138 (2018). https://doi.org/10.1021/acssensors.8b00701
14. X. Ma et al., Fast response room temperature amperometric gas sensors with modified Fe–N–C electrodes for ppb-level H_2S detection. ACS Appl. Nano Mater. **7**, 16649 (2024). https://doi.org/10.1021/acsanm.4c02716
15. H. Shang, H. Xu, Q. Liu, Y. Du, PdCu alloy nanosheets-constructed 3D flowers: new highly sensitive materials for H_2S detection. Sens. Actuators B Chem. **289**, 260 (2019). https://doi.org/10.1016/j.snb.2019.03.101
16. D. Mehta, D. Gupta, A. Kafle, S. Kaur, T.C. Nagaiah, Advances and challenges in nanomaterial-based electrochemical immunosensors for small cell lung cancer biomarker neuron-specific enolase. ACS Omega **9**, 33 (2023). https://doi.org/10.1021/acsomega.3c06388
17. B. Zhang, Z. Zhang, G. Li, Electrochemical biosensing methods for analysis of trace biomarkers: a review. Crit. Rev. Anal. Chem. (2025). https://doi.org/10.1080/10408347.2025.2479032
18. R. Singh, R. Gupta, D. Bansal, R. Bhateria, M. Sharma, A review on recent trends and future developments in electrochemical sensing. ACS Omega **9**, 7336 (2024). https://doi.org/10.1021/acsomega.3c08060
19. Z.-Y. Guo et al., Crystallinity engineering for overcoming the activity–stability tradeoff of spinel oxide in Fenton-like catalysis. PNAS **120**, e2220608120 (2023). https://doi.org/10.1073/pnas.2220608120
20. R. Nithya, S.S. Patil, H.P. Dasari, H. Dasari, S. Nethaji, Potential of $CoMn_2O_4$ spinel as soot oxidation catalyst and its kinetics thereof. Sci. Rep. **15**, 1174 (2025). https://doi.org/10.1038/s41598-025-85736-2
21. L. Lin, Q. Fu, R. Wang, T. Yao, X. Wang, B. Song, Spinel-type oxides for acidic oxygen evolution reaction: mechanism, modulation, and perspective. Adv. Energy Sustain. Res. **4**, 2300075 (2023). https://doi.org/10.1002/aesr.202300075
22. H. Chen, H. Chen, J. Chen, M. Song, Gas sensors based on semiconductor metal oxides fabricated by electrospinning: a review. Sensors **24**, 2962 (2024). https://doi.org/10.3390/s24102962
23. C. Shan, Y. Wang, J. Li, Q. Zhao, R. Han, C. Liu, Q. Liu, Recent advances of VOCs catalytic oxidation over spinel oxides: catalyst design and reaction mechanism. Environ. Sci. Technol. **57**, 9495 (2023). https://doi.org/10.1021/acs.est.2c09861
24. L. Zhao, C. Zhou, Y. Zhou, T. Wang, F. Liu, X. Yan, G. Lu, P. Sun, Simple preparation of yolk-shell $ZnCr_2O_4$ microspheres and their application to xylene gas sensor. Sens. Actuators, B Chem. **390**, 133929 (2023). https://doi.org/10.1016/j.snb.2023.133929
25. S. Mojumder, T. Das, S. Das, S. Das, M. Biswas, S. Ghosh, M. Pal, Spinel chromite MCr_2O_4 (M= Cu, Mg, Zn) nanoparticle-based sensors for trace acetone detection and noninvasive diabetes diagnosis from exhaled breath. ACS Appl. Nano Mater. **8**, 6188 (2025). https://doi.org/10.1021/acsanm.5c00561
26. V. Vinothkumar, Y.C. Sekhar, S.-M. Chen, G.V. Prasad, T.H. Kim, Fabrication of spinel MCr_2O_4 (M= Ni and Co) nanostructures as positive electrode materials for high-performance supercapacitors. J. Energy Storage **92**, 112185 (2024). https://doi.org/10.1016/j.est.2024.112185
27. S. Priyanka, K. Latha, $MnCr_2O_4$ nanocomposite modified carbon paste electrode based electrochemical sensor for determination of Norepinephrine: a cyclic voltammetry study. CDC **35**, 100769 (2021). https://doi.org/10.1016/j.cdc.2021.100769
28. S. Das, P.L. Mahapatra, P.P. Mondal, T. Das, M. Pal, D. Saha, A highly sensitive cobalt chromite thick film based trace acetone sensor with fast response and recovery times for the detection of diabetes from exhaled breath. Mater. Chem. Phys. **262**, 124291 (2021). https://doi.org/10.1016/j.matchemphys.2021.124291
29. B. Sriram, S. Kogularasu, S.-F. Wang, J.-K. Sheu, Deep eutectic solvent-mediated synthesis of spinel zinc chromite nanoparticles: a simple label-free electrochemical sensor for dopamine and ascorbic acid. ACS Appl. Nano Mater. **6**, 17593 (2023)
30. E. Sibanda, A. Prinsloo, C. Sheppard, P. Mohanty, Size effect on magnetic properties of $MnCr_2O_4$ nanoparticles. J. Magn. Magn. Mater. **558**, 169486 (2022). https://doi.org/10.1016/j.jmmm.2022.169486
31. P. Sharma, C. Das, S. Indris, T. Bergfeldt, L. Mereacre, M. Knapp, U. Geckle, H. Ehrenberg, M.S.D. Darma, Synthesis and characterization of a multication doped Mn spinel, $LiNi_{0.3}Cu_{0.1}Fe_{0.2}Mn_{1.4}O_4$, as 5V positive electrode material. ACS Omega **5**, 22861 (2020)
32. J.H. Lim, S.M. Lee, H.-S. Kim, H.Y. Kim, J. Park, S.-B. Jung, G.C. Park, J. Kim, J. Joo, Synergistic effect of indium and gallium co-doping on growth behavior and physical properties of hydrothermally grown ZnO nanorods. Sci. Rep. **7**, 41992 (2017). https://doi.org/10.1038/srep41992
33. H. Nesbitt, D. Banerjee, Interpretation of XPS Mn (2p) spectra of Mn oxyhydroxides and constraints on the mechanism of MnO_2 precipitation. Am. Mineral. **83**, 305 (1998). https://doi.org/10.2138/am-1998-3-414
34. A. Grosvenor, E. Bellhouse, A. Korinek, M. Bugnet, J. McDermid, XPS and EELS characterization of Mn_2SiO_4, $MnSiO_3$ and $MnAl_2O_4$. Appl. Surf. Sci. **379**, 242 (2016). https://doi.org/10.1016/j.apsusc.2016.03.235
35. M.C. Biesinger, B.P. Payne, A.P. Grosvenor, L.W. Lau, A.R. Gerson, R.S.C. Smart, Resolving surface chemical states in XPS analysis of first row transition metals, oxides and hydroxides: Cr, Mn, Fe, Co and Ni. Appl. Surf. Sci. **257**, 2717 (2011). https://doi.org/10.1016/j.apsusc.2010.10.051
36. J. Barreto, P.S. Bagus, F. Stavale, Multiplet XPS analysis of the Mn 2p for Mn_3O_4 thin films. J. Phys. Condens. Matter **37**, 045001 (2024). https://doi.org/10.1088/1361-648X/ad8b91
37. G.P. Halada, C.R. Clayton, Photoreduction of hexavalent chromium during X-ray photoelectron spectroscopy analysis of electrochemical and thermal films. J. Electrochem. Soc. **138**(10), 2921 (1991). https://doi.org/10.1149/1.2085340
38. D. Jin, H. Woo, S. Prabhakaran, Y. Lee, M.H. Kim, D.H. Kim, C. Lee, Single phase trimetallic spinel $CoCr_xRh_{2-x}O_4$ nanofibers for highly efficient oxygen evolution reaction under freshwater mimicking seawater conditions. Adv. Funct. Mater. **33**, 2301559 (2023). https://doi.org/10.1002/adfm.202301559
39. M.C. Biesinger, C. Brown, J.R. Mycroft, R.D. Davidson, N.S. McIntyre, X-ray photoelectron spectroscopy studies of chromium compounds. Surf. Interface Anal. **36**, 1550–1563 (2004). https://doi.org/10.1002/sia.1983
40. N.C. Maile et al., Electrochemical studies of $Ni(OH)_2$, NiO, and Ni_3S_2 nanostructures on Ni-foam toward binder-free positive electrode for hybrid supercapacitor application. Int. J. Energy Res. **46**, 22501 (2022). https://doi.org/10.1002/er.8553
41. P.S. Bagus, C.J. Nelin, C.R. Brundle, B.V. Crist, E.S. Ilton, N. Lahiri, K.M. Rosso, Main and satellite features in the Ni 2p XPS of NiO. Inorg. Chem. **61**, 18077 (2022)
42. J. Bai, S.-H. Han, R.-L. Peng, J.-H. Zeng, J.-X. Jiang, Y. Chen, Ultrathin rhodium oxide nanosheet nanoassemblies: synthesis, morphological stability, and electrocatalytic application. ACS Appl. Mater. Interfaces **9**, 17195 (2017)
43. Y. Abe, K. Kato, M. Kawamura, K. Sasaki, Rhodium and rhodium oxide thin films characterized by XPS. Surf. Sci. Spectra **8**, 117 (2001). https://doi.org/10.1116/11.20010801
44. S. Ghotekar, S. Pansambal, V.H. Nguyen, S. Bangale, K.Y.A. Lin, H.C.A. Murthy, R. Oza, Spinel $ZnCr_2O_4$ nanorods synthesized by facile sol–gel auto-combustion

method with biomedical properties. J. Sol-Gel Sci. Technol. **105**, 176 (2023). https://doi.org/10.1007/s10971-022-05964-0
45. Y. Wang, C. Hou, X. Lin, H. Jiang, C. Zhang, G. Liu, Dye degradation studies of hausmannite manganese oxide (Mn_3O_4) nanoparticles synthesized by chemical method. Appl. Phys. A **127**, 277 (2021). https://doi.org/10.1007/s00339-021-04428-6
46. S. Kirillov, V. Aleksandrova, T.V. Lisnycha, D. Dzanashvili, S. Khainakov, J. García, N. Visloguzova, O.I. Pendelyuk, Oxidation of synthetic hausmannite (Mn3O4) to manganite (MnOOH). J. Mol. Struct. **928**, 89 (2009). https://doi.org/10.1016/j.molstruc.2009.03.018
47. F. Fakhry, E. Shaheen, H. El-Dosoky, T. Meaz, M. Mubark, R. El-Shater, Elastic and magnetic characteristics of nano-spinel ferrite $Co_{0.5}$ $Mg_xCu_{0.5-x}Fe_2O_4$. Sci. Rep. **14**, 29407 (2024). https://doi.org/10.1038/s41598-024-74484-4
48. S. Chen, S. Jiang, Y. Rao, Y. Dong, J. Bu, Q. Yue, Reevesite with ordered intralayer atomic arrangement as an optimized nickel-iron oxygen evolution electrocatalyst. ChemElectroChem **8**, 558 (2021). https://doi.org/10.1002/celc.202100030
49. J. Lee, S. Choi, Y. Lee, PdCo composite nanoparticle-embedded N-doped carbon nanofibers for electrochemical carbon monoxide detection in physiological media. Diam. Relat. Mater. **160**, 113078 (2025). https://doi.org/10.1016/j.diamond.2025.113078
50. M.D. Brown, J.R. Hall, M.H. Schoenfisch, A direct and selective electrochemical hydrogen sulfide sensor. Anal. Chim. Acta **1045**, 67 (2019). https://doi.org/10.1016/j.aca.2018.08.054
51. N. Jeromiyas, V. Mani, P.-C. Chang, C.-H. Huang, K.N. Salama, S.-T. Huang, Anti-poisoning electrode for real-time in-situ monitoring of hydrogen sulfide release. Sens. Actuators, B Chem. **326**, 128844 (2021). https://doi.org/10.1016/j.snb.2020.128844
52. F. Paré, R. Castro, X. Guimera, G. Gabriel, M. Baeza, An inkjet-printed amperometric H_2S sensor for environmental applications. Chem. Proc. **5**, 4 (2021). https://doi.org/10.3390/CSAC2021-10462
53. S. Jeong, C. Song, J. Kim, Y. Lee, M.H. Kim, Rational synthesis of phosphorous rich iridium diphosphide (IrP_2) nanostructures for electrochemical H_2S detection. J. Alloys Compd. **947**, 169649 (2023). https://doi.org/10.1016/j.jallcom.2023.169649
54. X.-B. Hu, Y.-L. Liu, W.-J. Wang, H.-W. Zhang, Y. Qin, S. Guo, X.-W. Zhang, L. Fu, W.-H. Huang, Biomimetic graphene-based 3D scaffold for long-term cell culture and real-time electrochemical monitoring. Anal. Chem. **90**, 1136 (2018). https://doi.org/10.1021/acs.analchem.7b03324

Publisher's note

Springer Nature remains neutral with regard to jurisdictional claims in published maps and institutional affiliations.